

ORIGINAL ARTICLE

Open Access



# *In vitro* and *in vivo* optimized reconstruction for low-keV virtual monoenergetic photon-counting detector CT angiography of lower legs

Dirk Graafen<sup>1\*</sup> , Willi Bart<sup>1</sup>, Moritz C. Halfmann<sup>1,2</sup>, Lukas Müller<sup>1</sup>, Lukas Hobohm<sup>3,4</sup>, Yang Yang<sup>1</sup>, Achim Neufang<sup>5</sup>, Christine Espinola-Klein<sup>3,4</sup>, Michael B. Pitton<sup>1</sup>, Roman Kloeckner<sup>6</sup>, Akos Varga-Szemes<sup>7</sup> and Tilman Emrich<sup>1,2,7</sup>

## Abstract

**Background** Lower extremity peripheral artery disease frequently presents with calcifications which reduces the accuracy of computed tomography (CT) angiography, especially below-the-knee. Photon-counting detector (PCD)-CT offers improved spatial resolution and less calcium blooming. We aimed to identify the optimal reconstruction parameters for PCD-CT angiography of the lower legs.

**Methods** Tubes with different diameters (1–5 mm) were filled with different iodine concentrations and scanned in a water container. Images were reconstructed with 0.4 mm isotropic resolution using a quantitative kernel at all available sharpness levels (Qr36 to Qr76) and using different levels of quantum iterative reconstruction (QIR-2–4). Noise and image sharpness were determined for all reconstructions. Additionally, CT angiograms of 20 patients, reconstructed with a medium (Qr44), sharp (Qr60), and ultrasharp (Qr72) kernel at QIR-2-4, were evaluated by three readers assessing noise, delineation of plaques and vessel walls, and overall quality.

**Results** In the phantom study, increased kernel sharpness led to higher image noise (e.g., 16, 38, 77 HU for Qr44, Qr60, Qr72, and QIR-3). Image sharpness increased with increasing kernel sharpness, reaching a plateau at the medium-high level 60. Higher QIR levels decreased image noise (e.g., 51, 38, 25 HU at QIR-2–4 and Qr60) without reducing vessel sharpness. The qualitative *in vivo* results confirmed these findings: the sharp kernel (Qr60) with the highest QIR yielded the best overall quality.

**Conclusion** The combination of a sharpness level optimized reconstruction kernel (Qr60) and the highest QIR level yield the best image quality for PCD-CT angiography of the lower legs when reconstructed at 0.4-mm resolution.

**Relevance statement** Using high-resolution PCD-CT angiography with optimized reconstruction parameters might improve diagnostic accuracy and confidence in peripheral artery disease of the lower legs.

This article belongs to the thematic series entitled “Photon-counting CT: a disrupting innovation in medical imaging” (Guest Editors: Tilman Emrich (Mainz/Germany) and Akos Varga-Szemes (Charleston/US)).

\*Correspondence:

Dirk Graafen

[dirk.graafen@unimedizin-mainz.de](mailto:dirk.graafen@unimedizin-mainz.de)

Full list of author information is available at the end of the article



© The Author(s) 2024. **Open Access** This article is licensed under a Creative Commons Attribution 4.0 International License, which permits use, sharing, adaptation, distribution and reproduction in any medium or format, as long as you give appropriate credit to the original author(s) and the source, provide a link to the Creative Commons licence, and indicate if changes were made. The images or other third party material in this article are included in the article's Creative Commons licence, unless indicated otherwise in a credit line to the material. If material is not included in the article's Creative Commons licence and your intended use is not permitted by statutory regulation or exceeds the permitted use, you will need to obtain permission directly from the copyright holder. To view a copy of this licence, visit <http://creativecommons.org/licenses/by/4.0/>.

### Key Points

- Effective exploitation of the potential of PCD-CT angiography requires optimized reconstruction parameters.
- Too soft or too sharp reconstruction kernels reduce image quality.
- The highest level of quantum iterative reconstruction provides the best image quality.

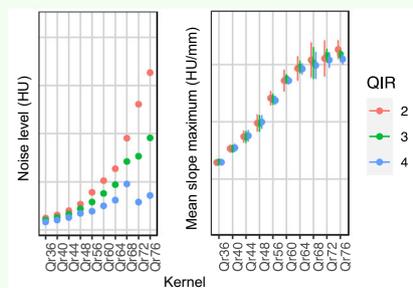
**Keywords** Below-the-knee, CT angiography, Photon-counting detector CT, Quantum iterative reconstruction, Reconstruction kernel

### Graphical Abstract

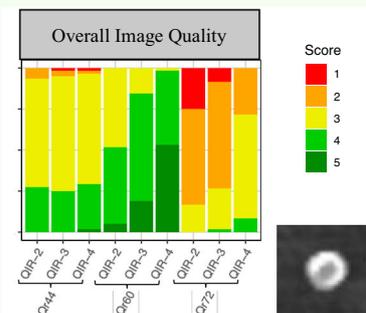
## *In vitro* and *in vivo* optimized reconstruction for low-keV virtual monoenergetic photon-counting detector CT angiography of lower legs

ESR<sup>®</sup> EUROPEAN SOCIETY OF RADIOLOGY

- Effective exploitation of the potential of PCD-CT angiography requires optimized reconstruction parameters.
- Too soft or too sharp reconstruction kernels reduce image quality.
- The highest level of quantum iterative reconstruction provides the best image quality.



Dependency of image noise and slope maximum on the reconstruction kernel and the quantum iterative reconstruction (QIR) level obtained from phantom measurement.



Qualitative image analysis of patient scans.

### High-resolution PCD-CT angiography with optimized reconstruction might improve diagnostic accuracy and confidence in peripheral artery disease of the lower legs

**Eur Radiol Exp (2024) Graafen D, Bart W, Halfmann MC, et al.**

**DOI: 10.1186/s41747-024-00481-x**

European  
Radiology  
EXPERIMENTAL

### Background

Lower extremity computed tomography (CT) angiography is a widely adapted medical imaging technique that enables the comprehensive evaluation of the peripheral vessels in individuals with peripheral artery disease, aneurysms, and trauma-related complications, and is used for both pre-interventional evaluation and postinterventional follow-up [1–3]. Previous studies reported a comparable diagnostic performance of CTA to digital subtraction angiography (DSA) [4, 5]. However, CTA diagnostic performance for the below-the-knee (BTK) arteries is typically limited due to their smaller vessel diameter, especially in combination with extensive arterial wall calcifications [6]. Despite those various developments in computed tomography (CT) technology, such as small field-of-view reconstructions [7], virtual monoenergetic image (VMI) reconstruction, and dual-energy CT-based calcium removal [8–10], have demonstrated improvements in imaging of the BTK

arteries, the diagnostic accuracy of CTA remains inferior to that of DSA.

A new generation of CT technology, based on a photon-counting detector (PCD), has recently received clinical approval. These PCDs are made of semiconductor crystals and have the unique capability of directly converting x-ray photons into electrical signals, allowing the detection and measurement of individual photons and their respective energies [11–13]. The PCD-CT technology offers several advantages over conventional energy-integrating detector (EID) CT, including improved dose efficiency, reduced image noise, and enhanced contrast-to-noise ratios [14–20]. Since the conversion process into optical photons is eliminated, PCDs do not require reflecting lamellae, therefore enabling improved spatial resolutions down to the submillimeter range. Additionally, PCDs enable inherently to capture spectral data. These advantages hold the potential to further improve BTK CTA.

While recent studies investigated the benefits of coronary PCD-CTA [21–25], studies on the lower extremity remain sparse. Two previous studies demonstrated improvements by PCD-CT over EID-CT for lower extremity CTA [26, 27] in which the impact of different keV levels of the VMIs or different radiation dose levels was investigated. Indeed, image quality further depends on additional parameters such as the reconstruction kernel, especially its sharpness level, and the strength level of the applied iterative reconstruction algorithm, which has not been investigated for run-off PCD-CTA so far. We hypothesized that exploiting the potential of PCD-CT to improve the image quality of run-off CTA crucially depends on the combination of these reconstruction parameters.

Therefore, the aim of this study was to identify the optimal reconstruction settings for PCD-CTA of the lower legs both in phantoms and patients.

## Methods

### Phantom study

#### Experimental setup

Two  $18.5 \times 12 \times 12$  cm plastic containers, filled to approximately 60% with water, were positioned side-by-side on the CT table to simulate the two lower legs. Silicone tubes with five different inner diameters (1, 2, 3, 4, and 5 mm) and a wall thickness of 1 mm were placed sequentially in the center of one of the water containers. To simulate different contrast agent concentrations, a serial dilution of an iodine contrast medium with an initial concentration of 370 mg I/mL (Ultravist 370, Bayer Vital, Leverkusen, Germany) was prepared. First, the contrast agent was diluted with saline by a factor of 1:10, which was the highest iodine concentration used for the experiments. Three additional steps with a dilution factor of 1:2 were performed. Together with a pure saline probe, this resulted in five different iodine concentrations: 37.0, 18.5, 9.25, 4.63, and 0 mg I/mL.

#### Imaging protocols

CT scans were performed with the first-generation clinical PCD-CT (NAEOTOM Alpha, Siemens Healthineers, Erlangen, Germany) with the software version Syngo CT VA40A. For every combination of the silicone tube and iodine concentration, scans with six different fixed tube currents (13, 25, 38, 50, 127, and 380 mAs) were acquired using a tube voltage of 120 kVp, resulting in the CT dose indices (CTDIs) of 1, 2, 3, 4, 10, and 30 mGy, respectively. All images were reconstructed as VMIs at 55 keV in the vascular spectral post-processing format, which is the vendor's standard keV level for CT angiographies and consistent with the recommendations of a previous study that investigated the effect of different keV levels [26]. The quantitative kernel (Qr) was applied with each

available sharpness level, *i.e.*, Qr36, Qr40, Qr44, Qr48, Qr56, Qr60, Qr64, Qr68, Qr72, and Qr76. The choice of the quantitative kernel instead of a vascular kernel was made because the Qr kernels were optimized for further spectral investigations such as plaque composition analysis. Every quantitative kernel was combined with three iterative reconstruction levels of the quantum iterative reconstruction (QIR) algorithm (QIR-2, QIR-3, and QIR-4), resulting in a total number of 30 reconstructions per dose level. A previous study demonstrated the inferiority of filtered back projection reconstructions (QIR-off) and first QIR level (QIR-1) for coronary PCD-CTA [21]. Therefore, they were not analyzed in this study. Images were reconstructed with a slice thickness of 0.4 mm, a  $512 \times 512$  matrix, and a field-of-view of  $205 \times 205$  mm<sup>2</sup> centered around the silicone tube. This yielded isotropic voxels with an edge length of 0.4 mm.

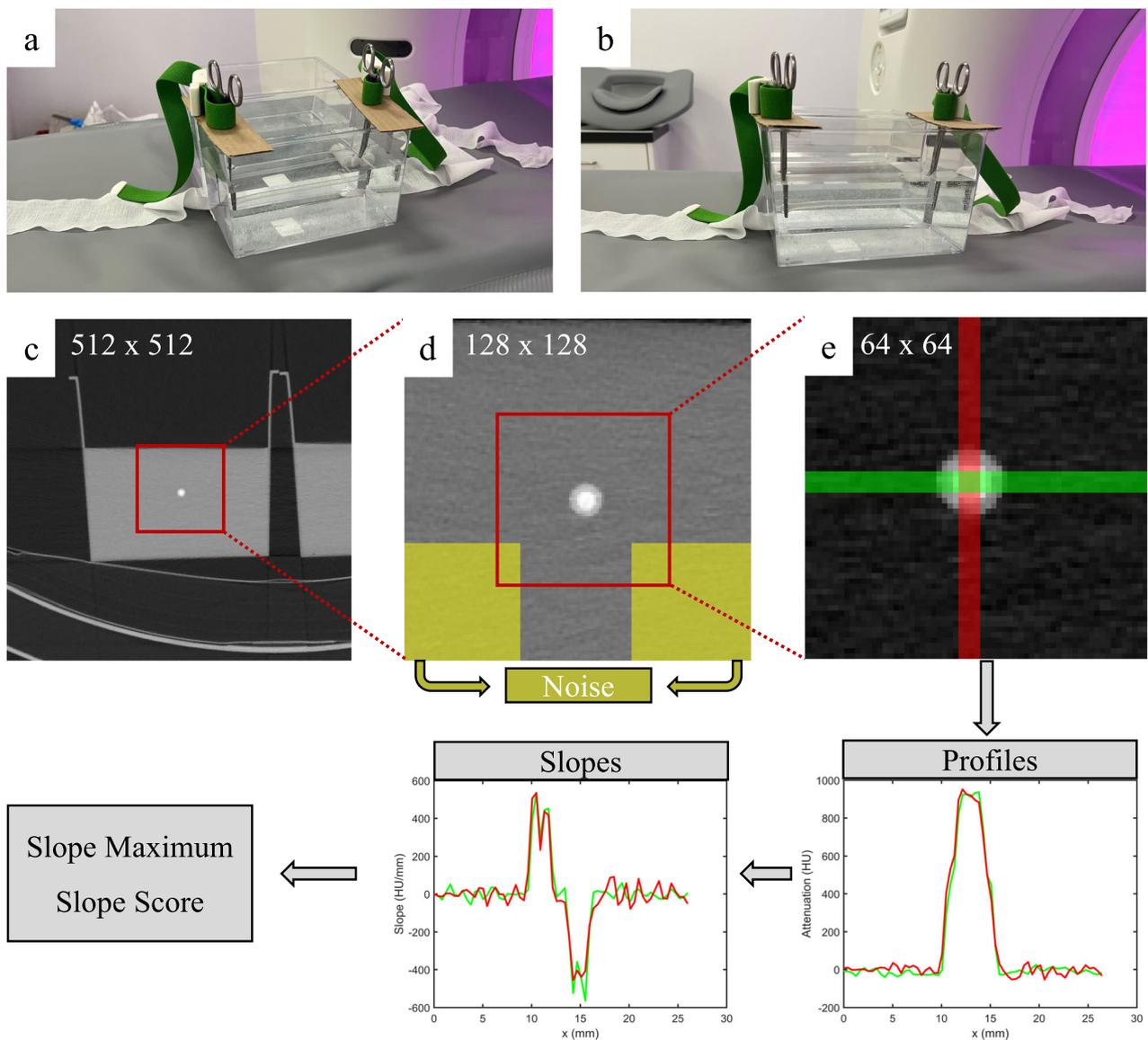
#### Image analysis

Image analyses were performed on the computing platform MATLAB (version R2021b, The MathWorks, Inc., Natick, USA). For each reconstruction, a single slice in the middle of the containers was used. First, these  $512 \times 512$  images were cropped to the  $128 \times 128$  central regions. In these, the noise levels were defined by the standard deviation of the water attenuation in the  $44 \times 44$  regions on the bottom left and bottom right. The images were cropped a second time to a  $64 \times 64$  region centered around the silicone tubes. Horizontal and vertical edge profiles were determined by averaging the attenuation of four neighboring pixels perpendicular to the profile direction. The amplitude of profiles was achieved by the maximum values and averages of the horizontal and vertical profiles. The slope at any point of these profiles was determined by the linear regression of each three neighboring points. The maximal slope values at the edges of the silicone pipe were determined, *i.e.*, at the transition from the water surrounding the wall or from the wall to the inner volume. The mean slope maximum was calculated by the mean of these four maxima. Additionally, a slope score was defined by the count of the local slope maxima, which were visible and above the noise level. This score could reach a maximum of eight when the slope of all four transitions from the surrounding water to the tube wall and of all four transitions from the pipe wall to the inner volume are visible as individual local maxima. Figure 1 illustrates the image analysis scheme.

#### In vivo study

##### Study population and imaging protocol

The study population consisted of 20 consecutive patients, who received a clinically indicated CTA of the lower extremities on a PCD-CT (NAEOTOM Alpha, Siemens) with the software version syngo CT VA40A SP1 in April and May



**Fig. 1** Image analysis scheme. **a, b** Photographs of the experimental setup. The initial images **(c)** are cropped centered **(d)** to determine image noise, and once again center cropped **(e)** for the extraction of the edge profiles and the slopes. The example shows the image of the silicone tube with an inner diameter of 3 mm filled with an iodine concentration of 37 mg I/mL. The slope score in this example is 8

2023. Images were acquired with a tube voltage of 120 kVp. Tube current modulation (CARE Dose4D, Siemens) was used with the image quality index set to 145. All images were reconstructed as VMIs at 55 keV with 0.4 mm isotropic voxels using a medium (Qr44), a sharp (Qr60), and an ultrasharp (Qr72) kernel. For each kernel, three different iterative reconstruction levels were applied (QIR-2, QIR-3, and QIR-4). Contrast media injection protocols consisted of a single bolus volume of 80 mL, with a flow of 4 mL/s and iodine flux of 1.5 gI/s (Ultravist® 370, Bayer Vital, Leverkusen, Germany) followed by a saline bolus volume of 40 mL, with a flow of

3 mL/s. Acquisitions were triggered by bolus tracking in the proximal abdominal aorta with a signal threshold of 100 HU.

#### Qualitative image analysis

Three readers rated the image quality—one board-certified consultant radiologist with 15 years and two residents with 2 and 4 years of experience in the field. For every patient, all nine reconstructed images (three kernels with three QIR levels, respectively) were arranged side-by-side in a random order using the institutional Picture Archiving and Communication System—PACS (Sectra®, Linköping, Sweden).

All images were anonymized and blinded for reconstruction parameters. Standard angiography window settings were used (width 1,100, level 300) with the possibility to change the windowing settings separately for each image. Consistent with previous studies [22, 24, 28], a 5-point Likert scale was used for the assessment of the following criteria: overall image quality (1: very poor/non-diagnostic, 2: poor, 3: moderate, 4: good, 5: excellent), image noise (1: very strong, 2: strong, 3: moderate, 4: little, 5: no/very little), and delineation of plaques and vessel walls (1: unacceptable/non-diagnostic, 2: suboptimal, 3: acceptable, 4: good, 5: precise).

### Statistical analysis

All statistical analyses were conducted using dedicated statistical software (R, version 4.1.1, R Foundation for Statistical Computing, Vienna, Austria). Categorical and binary baseline parameters were presented as absolute numbers and percentages, while ordinal-scaled variables were described using medians and interquartile ranges. For interval-scaled variables that followed a normal distribution according to the Shapiro–Wilk test, means and standard deviations were reported. To determine statistical differences in quantitative and qualitative image parameters, paired samples Wilcoxon rank tests with Bonferroni correction for multiple comparisons were used. A  $p$ -value  $< 0.050$  was considered statistically significant.

Inter-reader agreement was assessed using Krippendorff's  $\alpha$  coefficient with the following interpretation: poor agreement for values in the range of 0.0 to 0.2, fair agreement for values greater than 0.2 up to 0.4, moderate agreement for values greater than 0.4 up to 0.6, substantial agreement for values greater than 0.6 up to 0.8, and excellent (or near-perfect) agreement for values greater than 0.8 up to 1.0 [28].

## Results

### Phantom study

Noise levels for the different kernels, CTDIs, and QIR levels are shown in Fig. 2. Noise levels clearly increased when increasing kernel sharpness and keeping the radiation dose constant (e.g., at 3 mGy and using a QIR level of 3: noise level of 16 HU for Qr44, 38 HU for Qr60, and 77 HU for Qr72,  $p < 0.001$ ). Image noise showed an inverse relationship with increasing levels of QIR (e.g., at 3 mGy and reconstructed with the Qr60 kernel: noise level of 51 HU at QIR-2 versus 38 HU at QIR-3 versus 25 HU at QIR-4,  $p < 0.001$ ). The provided noise levels refer to the images with a 1 mm silicone tube filled with a 37 mg I/mL iodine solution. However, the tube diameter and the iodine concentration showed no relevant influence on the noise levels ( $p > 0.999$ ).

The dependency of the mean amplitude of the attenuation profile on kernel sharpness in the iodine-filled tubes is shown in Fig. 3. In the tubes with a diameter  $\leq 2$  mm, the mean amplitude is reduced in the images reconstructed with a soft kernel (e.g., at 3 mGy, 18.5 mg I/mL iodine solution, QIR-4, and 2 mm diameter: Qr36,  $787 \pm 12$  HU; Qr44,  $838 \pm 18$  HU; Qr60,  $940 \pm 39$  HU;  $p \leq 0.003$ ). This effect was not observed for the kernels with a sharpness level  $\geq 60$  ( $p > 0.999$ ). The results for the tubes filled with saline (0 mg I/mL) depict the mean amplitude of the silicone wall. Similar to the iodine-filled tubes, the mean wall amplitude was significantly reduced for kernel sharpness levels below 60 (e.g., at 3 mGy, QIR-4 and 2 mm diameter: Qr36,  $316 \pm 20$  HU; Qr44,  $387 \pm 15$  HU; Qr60,  $511 \pm 12$  HU;  $p < 0.001$ ).

Increased sharpness level of the kernel yielded higher slope maxima at the edges of the silicone tube—both at the outer edge to the saline surrounding and at the inner edge to the lumen (Fig. 4). While sharpness levels

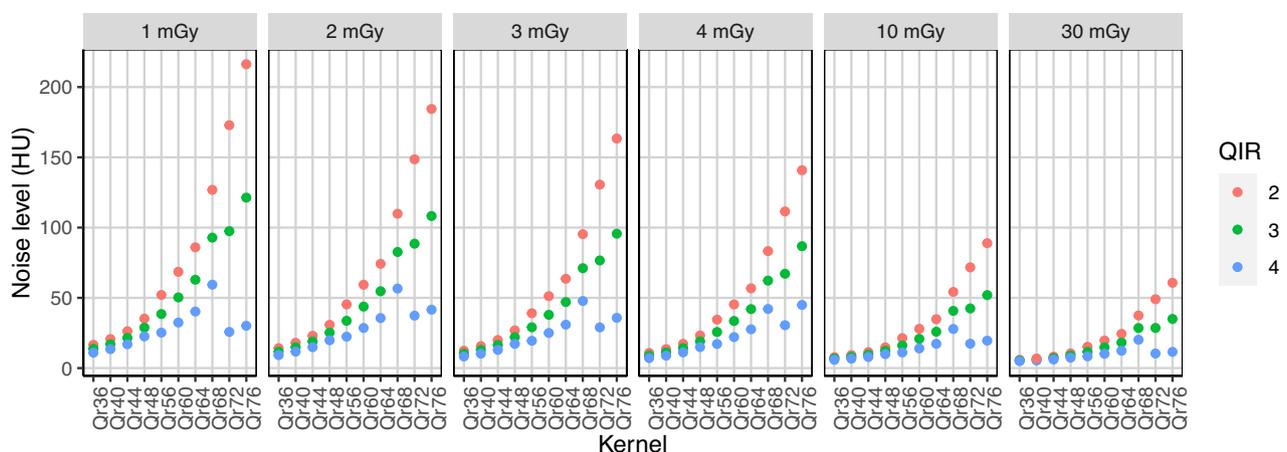


**Fig. 2** Dependence of image noise on the sharpness of the reconstruction kernel, the quantum iterative reconstruction (QIR) level, and the applied radiation dose. Noise levels are shown for the scans of the silicone tube with an inner diameter of 1 mm filled with an iodine concentration of 37 mg I/mL

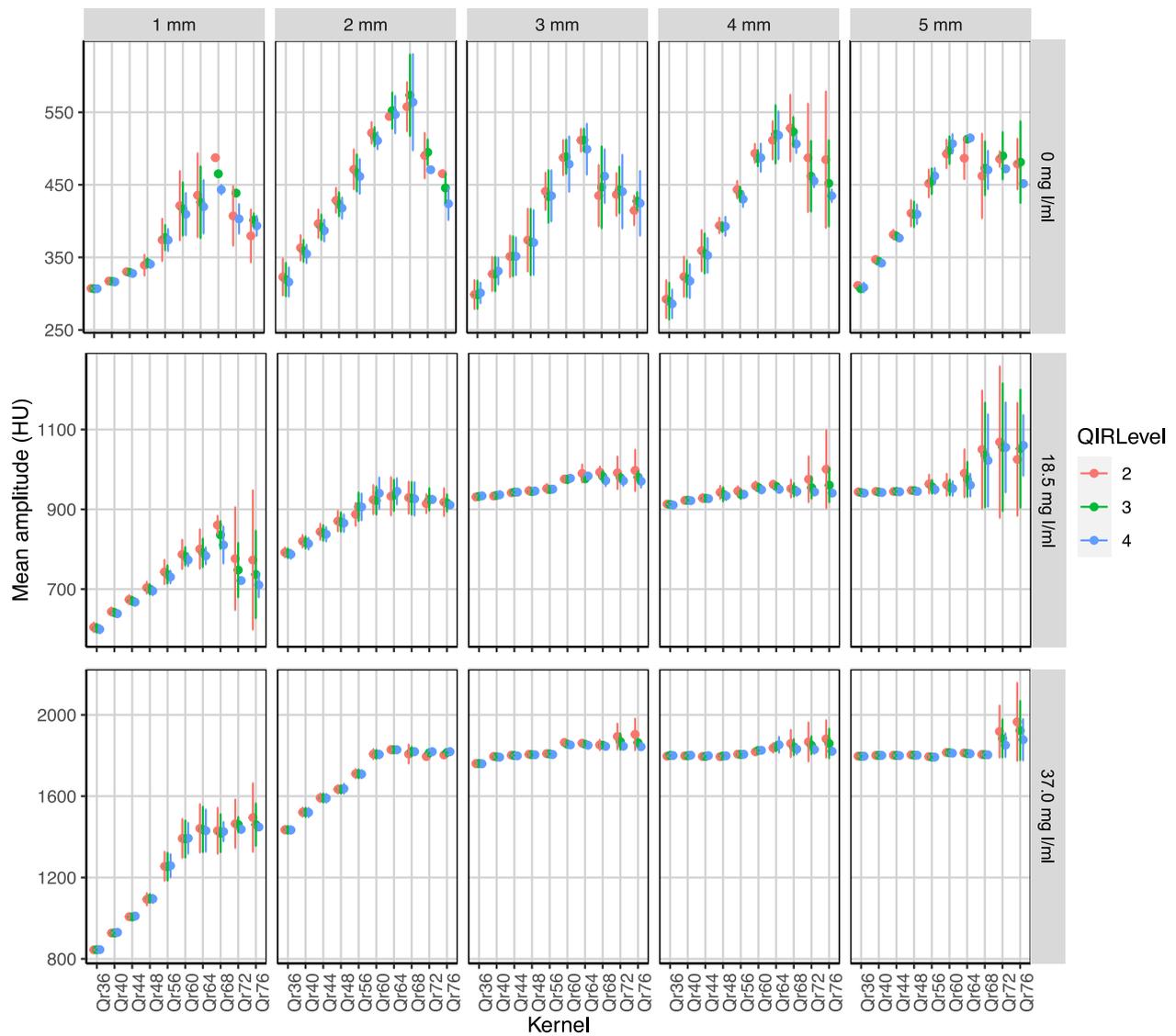


**Fig. 3** Dependency of the amplitude on the reconstruction kernel and the quantum iterative reconstruction (QIR) levels. Results are shown for the tube with five different inner diameters and three different iodine concentrations scanned with a CTDI of 3 mGy. The results for the concentration of 0 mg I/mL depict the amplitude of the tube wall. Dependency on the radiation dose is provided in the supplementary material

between 36 and 56 showed maximum slopes reduced by 16% to 47% of the maximum at sharpness level 76, maximum slopes of all kernels with sharpness level of 60 or higher differed by less than 10% (see Table 1). QIR had no significant influence on the maximum slope ( $p > 0.999$ ).

The results of the slope scores, which evaluate the slope maxima in relation to the noise level, are shown in the Supplementary Material (Figs. S1 to S5). In the images scanned with a CTDI of 3 mGy, typical CTDI at the BTK level, iodine yielded higher attenuation than the

vessel wall, therefore, soft kernels could not separate the two slope maxima at the tube wall. Kernels with higher sharpness levels overcame this restriction. However, caused by the increased noise level, ultrasharp kernels reached lower scores in several cases. Higher QIR levels improved the slope scores. These effects were even more pronounced in the images scanned with lower CTDIs. In contrast, higher CTDIs could partially overcome the limitations of ultrasharp kernels by the reduction of noise levels. In all acquired images with an iodine concentration of 9.25 mg I/mL (not shown in the figures),

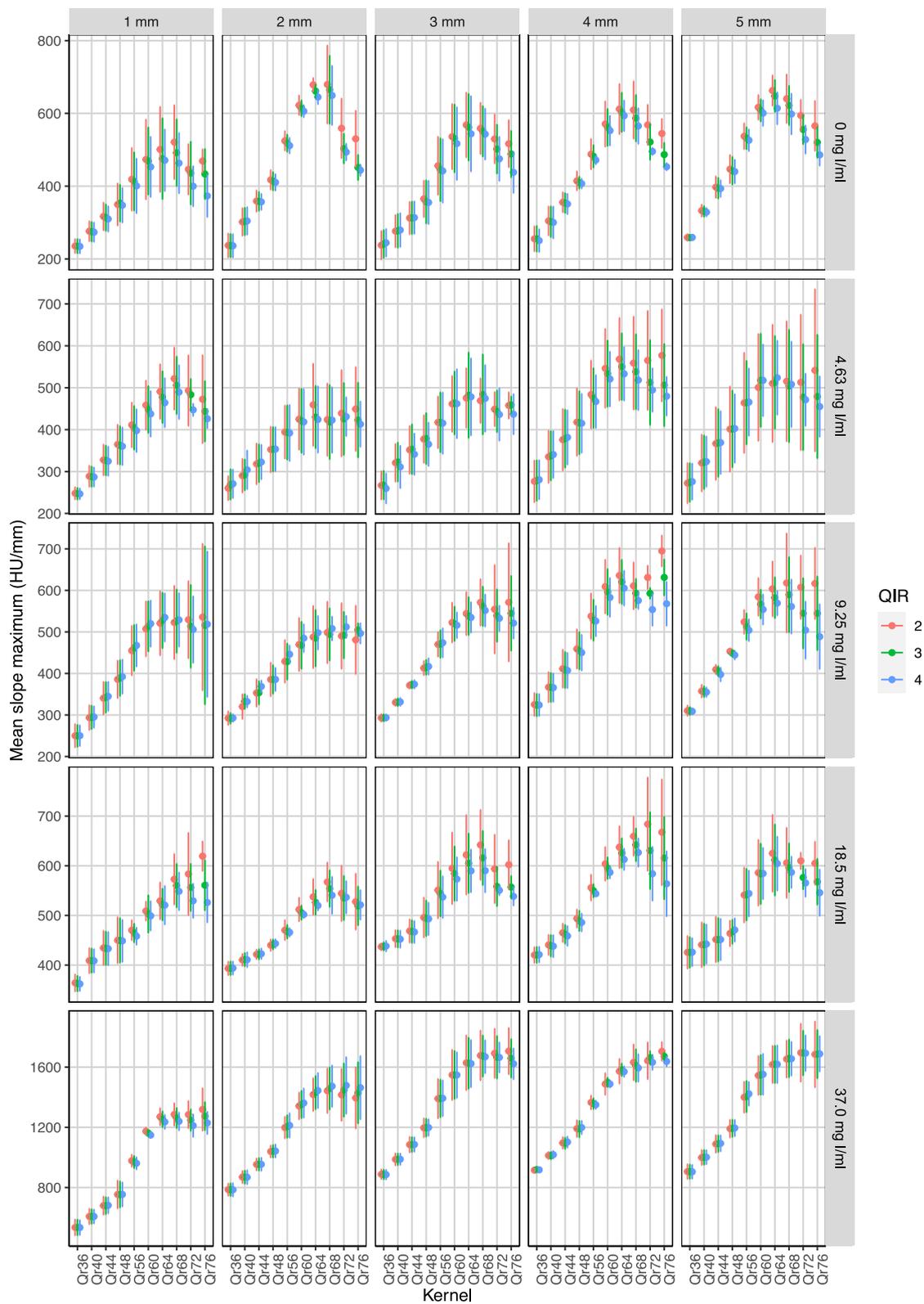


**Fig. 4** Dependency of the slope maximum on the reconstruction kernel for the different inner diameters and iodine concentrations. Results are shown for the tubes scanned with a CTDI of 3 mGy. The results of the other radiation doses are provided in the Supplementary material

**Table 1** Characteristics of the modulation transfer functions (MTF) and maximum slopes for the 5-mm tube filled with 37 mg I/mL and scanned with a CTDI of 3 mGy and QIR-4

Kernel	$\rho_{50}$ (Lp/ cm)	$\rho_{10}$ (Lp/ cm)	Maximum slope (HU/mm)	Relative difference to Qr76
Qr36	3.4	5.6	900 ± 50	-47%
Qr40	4.0	6.6	1,000 ± 50	-41%
Qr44	4.6	7.7	1,090 ± 50	-35%
Qr48	5.4	9.0	1,200 ± 50	-29%
Qr56	7.4	10.8	1,420 ± 80	-16%
Qr60	8.8	11.2	1,550 ± 140	-9%
Qr64	10.1	11.2	1,620 ± 130	-4%
Qr68	11.8	13.9	1,660 ± 110	-2%
Qr72	14.1	17.3	1,690 ± 120	0%
Qr76	15.8	18.7	1,690 ± 120	0%

$\rho_{50}$  and  $\rho_{10}$  represent the spatial frequencies at which the MTF decreases to 50% and 10% of its value at  $\rho = 0$  Lp/cm. Mean data with a standard deviation of the maximum slope is presented. Lp Line pairs

**Table 2** Baseline characteristics ( $n = 20$ )

Age (years)	67 (63–80)	
Male sex ( $n$ )	16 (80%)	
Body height (cm)	174.5 (170–178)	
Body weight (kg)	78.0 (73.5–85.8)	
Body Mass Index (kg/m <sup>2</sup> )	25.6 (24.2–28.1)	
Patients with peripheral artery disease ( $n$ )	18	
Fontaine stage ( $n$ )		
IIa	1	
IIb	8	
III	3	
IV	6	
Patients with plaques in the evaluated regions ( $n$ )	15	
Patients with ( $n$ )	Popliteal	BTK
Calcified plaques	9	11
Noncalcified plaques	5	8
Mixed plaques	9	7

Median data is shown with interquartile ranges in parentheses. BTK Below-the-knee

slope scores reached only a value of 4, since the attenuation difference of the silicone wall and iodine was too small to separate a local slope maximum.

### In vivo study

The baseline characteristics of the 20 patients scanned in this study are listed in Table 2. The median effective CTDI in the lower leg area was 2.51 mGy (2.50–2.57).

Table 3 and Fig. 5 showcase the outcome of the qualitative image analysis. No relevant differences were seen between the two evaluated levels (popliteal and BTK),

even though the small difference in the delineation reached statistical significance ( $p = 0.040$ ). All three readers found increasing noise levels (lower scores) with an increase in the kernel sharpness. For all three kernels, an effective reduction of noise was seen by the increase of the QIR level ( $p < 0.050$ ). By the increase of the QIR level from 2 to 4, the image noise changed from little (score 4) to very little (score 5) for the medium kernel (Qr44), from moderate (score 3) to little (score 4) for the sharp kernel (Qr60), and from very strong (score 1) to strong (score 2) for the ultrasharp kernel (Qr72).

The images reconstructed with the sharp kernel (Qr60) reached the highest scores in the delineation of plaques and vessel walls. The delineation in these images was predominantly classified as good (score 4), whereas in the other images, it was rated suboptimal (score 2) to acceptable (score 3). None of the three readers observed any reduction in delineation caused by the QIR algorithm, e.g., due to blurring effects. In contrast, images with QIR-4 reached even higher scores ( $p < 0.050$ ), probably caused by the reduction of image noise.

The images reconstructed with the sharp kernel reached the best scores in the delineation of the plaques and vessel walls (for the pair-wise comparisons with Qr60 QIR-4 all  $p \leq 0.001$ , except to Qr60 QIR-3 with  $p = 0.298$  on the popliteal and  $p = 0.307$  on the BTK level). The overall image quality of the sharp kernels with the highest QIR level (QIR-4) was rated best with good to excellent scores (for the pair-wise comparisons with Qr60 QIR-4, all  $p \leq 0.002$ ).

Altogether, inter-rater reliability was substantial ( $\alpha = 0.71$  for the popliteal, and 0.70 for the BTK level). Looking at the individual criteria, an excellent agreement was found for image noise (popliteal,  $\alpha = 0.86$ ; BTK,  $\alpha = 0.84$ ), a moderate agreement for delineation of plaques and vessel walls (popliteal,  $\alpha = 0.53$ ; BTK,  $\alpha = 0.52$ ), and a substantial agreement for overall image quality (popliteal,  $\alpha = 0.66$ ; BTK,  $\alpha = 0.68$ ).

Image examples reconstructed with the different kernels and QIR levels are shown in Figs. 6 and 7.

### Discussion

In this *in vitro* study with *in vivo* validation, optimal reconstruction parameters for PCD-CTA images of the BTK arteries were defined. A sharp reconstruction kernel (Qr60) in combination with the highest available QIR level (QIR-4) provided the best image quality for arterial plaque analysis without suffering from image blurring or excessive noise levels.

Enhancing the diagnostic accuracy of lower extremity CTA holds significant clinical importance, given its widespread adoption as a standard procedure for assessing patients with peripheral arterial disease [2, 29]. It is

**Table 3** Median scores of qualitative image analyses

Reconstruction		Image noise		Delineation of plaques and vessel walls		Overall image quality	
		Popliteal	BTK	Popliteal	BTK	Popliteal	BTK
Qr44	QIR-2	4 (4–4)	4 (4–4)	3 (2–3)	2 (2–3)	3 (3–4)	3 (3–3)
	QIR-3	5 (4–5)	5 (4–5)	3 (2–3)	2 (2–3)	3 (3–3)	3 (3–3)
	QIR-4	5 (5–5)	5 (5–5)	3 (2–3)	2 (2–3)	3 (3–4)	3 (3–3)
Qr60	QIR-2	3 (3–3)	3 (3–3)	4 (3–4)	4 (3–4)	4 (3–4)	3 (3–4)
	QIR-3	3 (3–4)	3 (3–4)	4 (4–5)	4 (4–4)	4 (4–4)	4 (4–4)
	QIR-4	4 (4–4)	4 (4–4)	5 (4–5)	4 (4–5)	5 (4–5)	4 (4–5)
Qr72	QIR-2	1 (1–2)	1 (1–2)	2 (2–3)	2 (2–3)	2 (2–2)	2 (2–2)
	QIR-3	2 (1–2)	2 (1–2)	3 (2–3)	2 (2–3)	2 (2–3)	2 (2–3)
	QIR-4	2 (2–3)	2 (2–3)	3 (2–3)	3 (2–3)	3 (2–3)	3 (2–3)

Interquartile ranges are presented in parentheses. *BTK* Below-the-knee, *Pop* Popliteal

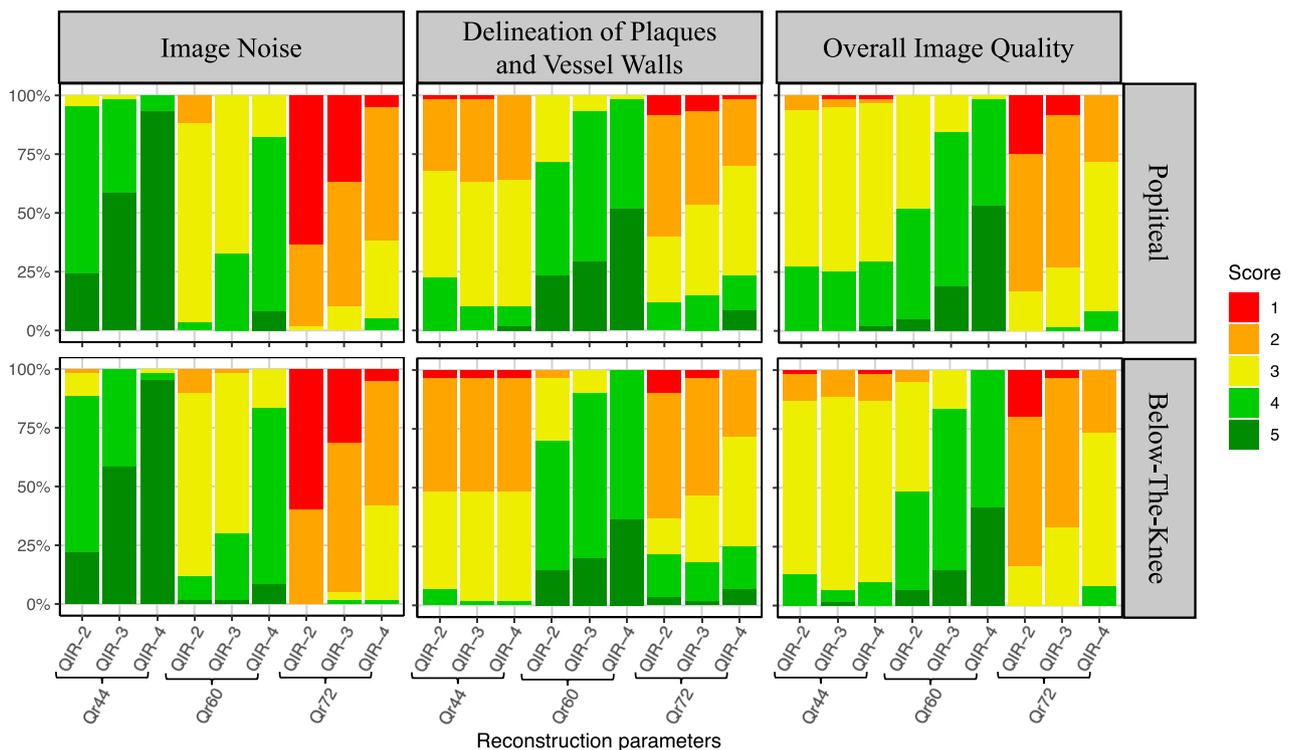


**Fig. 5** Qualitative image analyses of image noise, delineation of plaques and vessel walls, and overall CTA image quality at the popliteal (Pop) and below-the-knee (BTK) levels

increasingly being utilized to guide treatment decisions (surgical *versus* transluminal) and interventional treatment planning [30, 31]. However, the assessment of small BTK vessels with a high prevalence of arteriosclerosis remains challenging [6, 32]. Salimova et al [7] showed an image quality improvement of the BTK level by small field-of-view reconstructions due to a higher in-plane spatial resolution. Additional improvements could be

reached by utilizing dual-energy CT with its spectral capabilities such as VMIs or calcium removal [8–10]. Despite these advances, dual-energy CT still exhibits lower diagnostic accuracy when compared to DSA, especially in the BTK arteries.

Two preliminary studies investigated the potential of PCD-CTA in the lower extremities [26, 27]. Both studies used a 2.5-fold higher slice thickness of 1 mm, compared

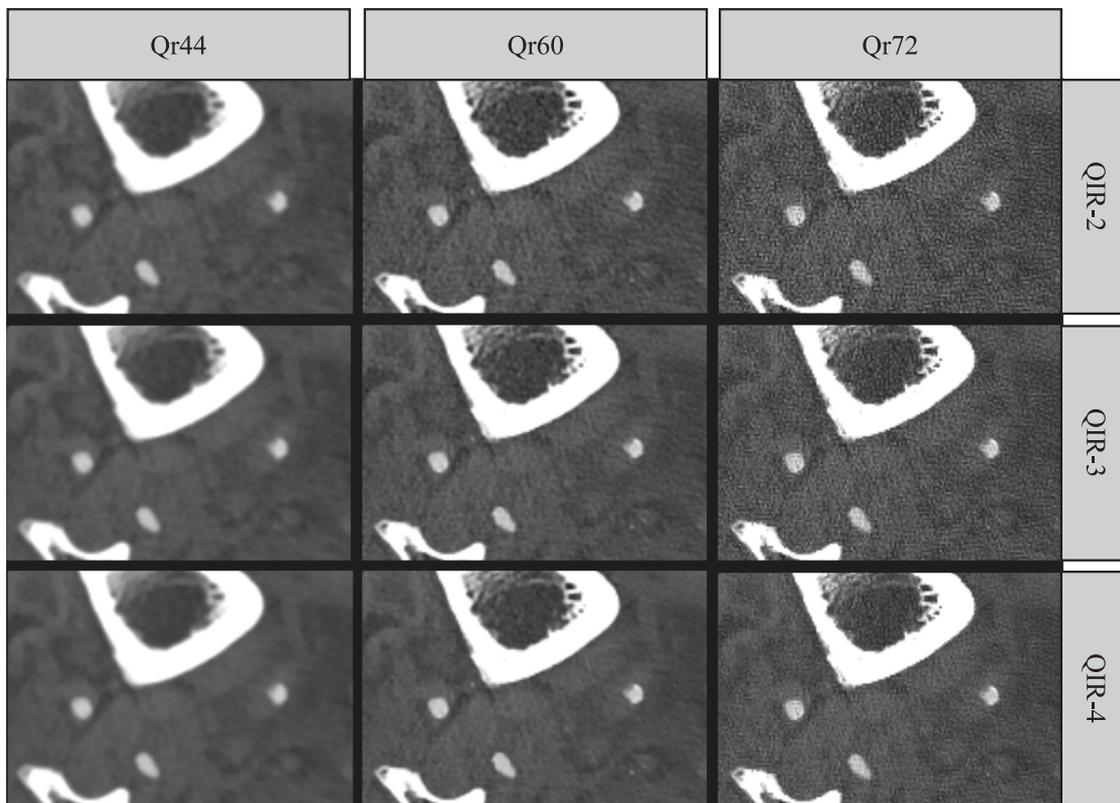


**Fig. 6** Image example at the below-the-knee level. The example shows a noncalcified plaque of the posterior tibial artery of an 80-year-old male patient who had a wet necrosis of the right heel. The images are reconstructed with the medium (Qr44), sharp (Qr60), and ultrasharp (Qr72) kernel, and with three different levels of the quantum iterative reconstruction algorithm (QIR-2 to QIR-4). Window settings: width 1,500; level 600

to our study. Rippel et al [26] analyzed the effect of different keV levels of the VMIs reconstructed with manually adapted fields of view with an estimated in-plane resolution between  $0.6 \times 0.6$  and  $0.7 \times 0.7 \text{ mm}^2$ , Qr36 kernel, and QIR-3. Their study shows that using low-keV VMI reconstructions yields considerably improved contrast-to-noise ratios compared to 80 kVp and 100 kVp EID-CT acquisitions, all while maintaining consistent subjective image quality. Gruschwitz et al [27] analyzed the benefit of PCD-CTA using a cadaveric upper leg model with images reconstructed with a slice thickness of 1 mm and an in-plane resolution of  $0.3 \times 0.3 \text{ mm}^2$  using the Bv48 kernel and QIR-3. They demonstrated the potential to achieve up to an 83% reduction in radiation exposure compared to EID-CT, while also offering enhanced luminal contrast attenuation, noise reduction, and improved image quality. However, even more pronounced benefits of PCD-CTA could be expected using the optimized reconstruction parameters identified in our study.

Thus far, spectral reconstructions on the PCD-CT scanner, such as VMIs or material decomposition, are

limited to a slice thickness of 0.4 mm or higher. For this reason, the images were reconstructed as 0.4 mm isotropic voxels and with the quantitative kernels (Qr), which are specifically designed for optimizing spectral post-processing, ensuring the provision of highly stable data, particularly for tasks such as plaque composition analysis [33]. This might provide both prognostic imaging biomarkers and predictors for therapy success for BTK plaques, as was shown in previous studies for superficial femoral artery occlusions, *e.g.*, in an MRI study by McDermott et al [34], and in a study by Hartwig et al, who used plaque analysis with optical coherence tomography [35].

In the applied standard acquisition mode, the maximum in-plane spatial resolution, given by the size of the detector elements, is 0.2 mm [36]. Since the used voxel size of 0.4 mm exceeds this value, it determines the maximum possible spatial frequency of the reconstruction. According to the Nyquist theorem, the maximum spatial frequency  $\rho_{\text{max}}$  is 12.5 Lp/cm. To exhaust the given spatial resolution, the reconstruction kernel must not suppress these high spatial frequencies, *i.e.*, its modulation

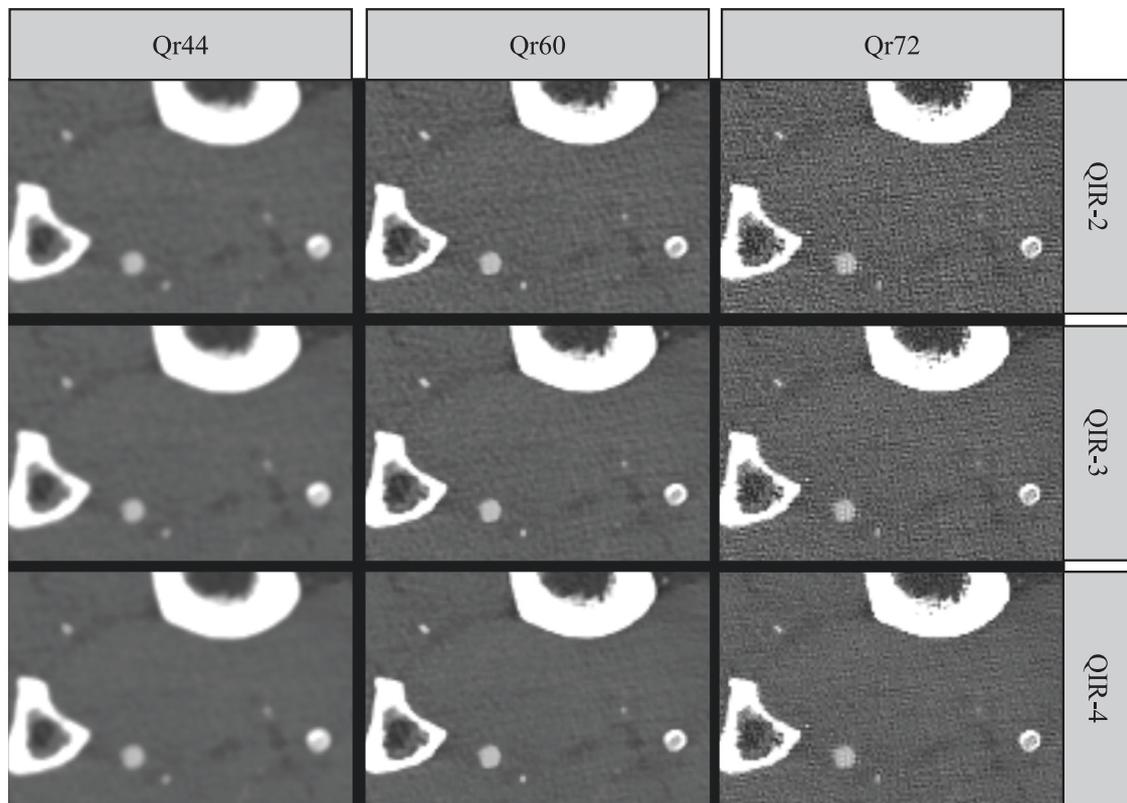


**Fig. 7** Image example at the below-the-knee level. The example shows a circular calcification of the posterior tibial artery and an occlusion of the anterior tibial artery of a 69-year-old female patient who had Fontaine stage IIb of peripheral artery disease. The images are reconstructed with the medium (Qr44), sharp (Qr60), and ultrasharp (Qr72) kernel, and with three different levels of the quantum iterative reconstruction algorithm (QIR-2 to QIR-4). Window settings: width 1,500; level 500

transfer function should not be significantly reduced in this specific frequency range [22]. Softer kernels than the optimum kernel suppress these spatial frequencies too much and lead to a blurring of the image with reduced delineation of edges at the vessel walls or the plaque borders. This effect could be seen in our results for both the mean amplitude (see Fig. 3) and the mean slope maximum (see Fig. 4), which were reduced for kernels that were too soft. The results of the slope scores (c.f. supplementary material) also show this effect. Especially for higher iodine concentrations, soft kernels lead to a blooming of the inner tube volume, whereby the tube wall is overlaid and the boundary to the surrounding area can no longer be demarcated. This resulted in reduced slope scores for higher iodine concentrations and softer kernels. On the other side, ultrasharp kernels have the potential to transfer even higher spatial frequencies. However, because the voxel size determines the maximum spatial frequency, the utilization of ultrasharp kernels primarily results in amplified image noise without providing substantial improvements in image sharpness. In the case of 0.4 mm isotropic voxels, the  $\rho_{10}$  values of the kernels Qr68 to Qr76,

*i.e.*, the spatial frequency at which the modulation transfer function value drops to 10% of its value at  $\rho = 0$  Lp/cm [22], exceed the maximum spatial frequency  $\rho_{\max}$  (see Table 1). This mainly explains some nonlinear results observed with these kernel sharpnesses, for example, the decrease of the noise (see Fig. 2) and the decrease of the mean amplitude (see Fig. 3), which is accompanied by a reduction of the mean maximum slope (see Fig. 4).

Waiving spectral capabilities, the PCD-CT scanner allows for higher spatial resolutions using ultrahigh resolution (UHR) mode with a slice thickness down to 0.2 mm. An improvement of the spatial resolution requires an increase in the kernel sharpness to fully exploit these enhancements. Potentially, the usage of dedicated edge-attenuating kernels, like the vascular kernels Bv, might further improve the delineation of vessel walls and plaques. Mergen et al [22] identified the Bv64 kernel to optimize UHR coronary PCD-CTA with non-isotropic voxels with 0.2 mm slice thickness and  $0.4 \times 0.4 \text{ mm}^2$  in-plane resolution. However, these results are not directly transferable to lower extremity PCD-CTA, since in coronary PCD-CTA the periodic

movement of the heart requires ECG triggering or gating which influences the reconstruction procedure. In addition, the UHR mode with 0.2 mm slice thickness typically requires higher radiation doses to compensate for increased image noise. The advantages in diagnostic certainty and treatment allocation of UHR PCD-CTA must be demonstrated in future studies to justify the applications of higher radiation doses in routine clinical practice. In contrast to the UHR mode, the diagnostic power of the standard resolution mode down to a slice thickness of 0.4 mm could be further improved by more pronounced exploitation of spectral capabilities such as iodine maps or a vascular calcium removal algorithm [37].

In comparison to DSA, Meyer et al [6] reported a reduction of sensitivity and specificity in the grading of steno-occlusive lesions with increased calcification using conventional CTA with a slice thickness of 2 mm. As shown in this study, PCD-CTA with optimized reconstruction parameters yields improved delineation of plaques. Therefore, clearly reduced blooming artifacts are expected with the potential of improved qualitative and quantitative diagnosis overcoming the restrictions of increased calcifications. An alternative modality for the imaging of the BTK and pedal arteries is contrast-enhanced magnetic resonance angiography. Its advantages are the capability to conduct multiphasic imaging comparable to DSA, eliminating exposure to ionizing radiation, and achieving this with a minimal amount of contrast material [38]. However, the spatial resolution of contrast-enhanced magnetic resonance angiography does not reach that of PCD-CTA, since even high-resolution protocols are limited to isotropic voxels with an edge length around 1 mm [39–41]. In addition to the existing advantages of CTA such as rapid acquisition and direct visualization of classified plaques, PCD-CTA provides more technical advantages with spectral imaging and UHR acquisition. However, the clinical benefits of these technical improvements need to be proven in further studies.

This study has a few limitations which merit consideration. First, the study was conducted at a single center and the scope of the *in vivo* part of the study was only to preliminarily validate the phantom results, therefore the patient sample size and the number of evaluated plaques were limited. Second, only the quantitative kernel Qr was used. More edge-attenuating kernels might be beneficial under certain circumstances. In a previous study of coronary PCD-CTA, the vascular kernel Bv was preferred over the Qr kernel [28]. Third, VMIs were exclusively reconstructed at 55 keV, which is consistent with the results of the keV level modification by Rippel et al [26]. However, a recent phantom study for coronary PCD-CTA reports the best image quality for the 40 keV VMI level [21]. Even though 40 keV VMIs might further

improve image quality, the results of the study concerning the kernel sharpness and the QIR level are expected not to be influenced relevantly by this change in keV level. Fourth, only the three highest QIR levels were considered and FBP was not used as the reference standard. Fifth, CTA images were assessed without comparison to DSA as an invasive reference.

In conclusion, for isotropic voxels with 0.4-mm edge length, a sharp kernel (Qr60) should be used for PCD-CTA of the lower legs. The highest QIR level provides the most effective dose reduction without quality reduction by image blurring. This optimal choice of kernel sharpness and QIR level is necessary for effectively exploiting the potential of PCD-CT for CTA of the lower legs.

#### Abbreviations

BTK	Below-the-knee
CT	Computed tomography
CTA	CT angiography
CTDI	CT dose index
DSA	Digital subtraction angiography
EID	Energy-integrating detector
PCD	Photon-counting detector
QIR	Quantum iterative reconstruction
UHR	Ultrahigh resolution
VMI	Virtual monoenergetic image

#### Supplementary information

The online version contains supplementary material available at <https://doi.org/10.1186/s41747-024-00481-x>.

**Additional file 1: Supplementary Fig. S1.** Dependency of the amplitude on the reconstruction kernel, the quantum iterative reconstruction (QIR) levels, and the radiation dose. Results are shown for the tube with five different inner diameters and three different iodine concentrations. The results for the concentration of 0 mg I/ml depict the amplitude of the tube wall. **Supplementary Fig. S2.** Dependency of the slope maximum on the reconstruction kernel for the different inner diameters and iodine concentrations. **Supplementary Fig. S3.** Slope scores for a CT dose index of 1 mGy. Results are shown for the different sharpness levels of the reconstruction kernel, the different Quantum iterative reconstruction (QIR) levels, the different inner diameters of the silicone pipes and the different iodine concentrations. **Supplementary Fig. S4.** Slope scores for a CT dose index of 2 mGy. Results are shown for the different sharpness levels of the reconstruction kernel, the different Quantum iterative reconstruction (QIR) levels, the different inner diameters of the silicone pipes and the different iodine concentrations. **Supplementary Fig. S5.** Slope scores for a CT dose index of 3 mGy. Results are shown for the different sharpness levels of the reconstruction kernel, the different Quantum iterative reconstruction (QIR) levels, the different inner diameters of the silicone pipes and the different iodine concentration. **Supplementary Fig. S6.** Slope scores for a CT dose index of 4 mGy. Results are shown for the different sharpness levels of the reconstruction kernel, the different Quantum iterative reconstruction (QIR) levels, the different inner diameters of the silicone pipes and the different iodine concentrations. **Supplementary Fig. S7.** Slope scores for a CT dose index of 10 mGy. Results are shown for the different sharpness levels of the reconstruction kernel, the different Quantum iterative reconstruction (QIR) levels, the different inner diameters of the silicone pipes and the different iodine concentrations. **Supplementary Fig. S8.** Slope scores for a CT dose index of 30 mGy. Results are shown for the different sharpness levels of the reconstruction kernel, the different Quantum iterative reconstruction (QIR) levels, the different inner diameters of the silicone pipes and the different iodine concentrations.

### Acknowledgements

This study contains parts of the doctoral thesis of one of the authors (WB). Large language models were not used.

### Authors contributions

Conceptualization, DG, LM, YY, RK, AVS, and TE; methodology, DG, and WB; software, DG; validation, DG, WB, MCH, LM, YY, RK, AVS, and TE; formal analysis, DG and WB; investigation, DG and WB; resources, TE; data curation, DG; writing—original draft preparation, all authors; writing—review and editing, all authors; visualization, DG, WB, MCH, LM, and YY; supervision, RK, AVS, and TE; project administration, DG; funding acquisition—no funding. All authors have read and agreed to the published version of the manuscript.

### Funding

This research received no external funding. Open Access funding enabled and organized by Projekt DEAL.

### Data availability

The datasets used and/or analyzed during the current study are available from the corresponding author upon reasonable request.

### Declarations

#### Ethics approval and consent to participate

This retrospective study was approved by the local ethics committee of Rhineland-Palatinate. Informed consent was waived by the ethics committee (Reg. Nr. 2022-16359).

#### Consent for publication

Not applicable.

#### Competing interests

DG and RK received speaking fees from Siemens Healthineers. TE reports an advisory board membership of Siemens Healthineers and received speaking fees and travel reimbursement from Siemens Healthineers. DG, WB, MCH, LM, YY, and TE receive institutional research support from Siemens Healthineers. AVS received research support from Siemens and consulting fees from Bayer and Elucid Bioimaging. TE and DG are members of the Scientific Editorial Board (Computed Tomography, the former additionally being that section editor) and AVS is a Deputy Editor for *European Radiology Experimental*. They have not participated in the selection nor review processes for this article. All other authors have no competing interests to declare.

#### Author details

<sup>1</sup>Department of Diagnostic and Interventional Radiology, University Medical Center of the Johannes Gutenberg-University Mainz, Mainz, Germany. <sup>2</sup>German Center for Cardiovascular Research (DZHK), Partner-Site Rhine-Main, Mainz, Germany. <sup>3</sup>Department of Cardiology, University Medical Center of the Johannes Gutenberg-University Mainz, Mainz, Germany. <sup>4</sup>Center for Thrombosis and Hemostasis (CTH), University Medical Center of the Johannes Gutenberg-University Mainz, Mainz, Germany. <sup>5</sup>Department of Cardiac and Vascular Surgery, University Medical Center of the Johannes Gutenberg-University Mainz, Mainz, Germany. <sup>6</sup>Institute of Interventional Radiology, University Hospital Schleswig-Holstein, Campus Lübeck, Lübeck, Germany. <sup>7</sup>Division of Cardiovascular Imaging, Department of Radiology and Radiological Science, Medical University of South Carolina, Charleston, SC, USA.

Received: 11 September 2023 Accepted: 6 February 2024

Published online: 01 August 2024

### References

- Met R, Bipat S, Legemate DA et al (2009) Diagnostic performance of computed tomography angiography in peripheral arterial disease: a systematic review and meta-analysis. *JAMA* 301:415–424. <https://doi.org/10.1001/JAMA.301.4.415>

- Baliyan V, Shaqdan K, Hedgire S, Ghoshhajra B (2019) Vascular computed tomography angiography technique and indications. *Cardiovasc Diagn Ther* 9:S14. <https://doi.org/10.21037/CDT.2019.07.04>
- Shwaiki O, Rashwan B, Fink MA et al (2021) Lower extremity CT angiography in peripheral arterial disease: from the established approach to evolving technical developments. *Int J Cardiovasc Imaging* 37:3101–3114. <https://doi.org/10.1007/S10554-021-02277-1>
- Albrecht T, Foert E, Holtkamp R et al (2007) 16-MDCT angiography of aortoiliac and lower extremity arteries: comparison with digital subtraction angiography. *AJR Am J Roentgenol* 189:702–711. <https://doi.org/10.2214/AJR.07.2333>
- Heijenbrok-Kal MH, Kock MCJM, Hunink MGM (2007) Lower extremity arterial disease: multidetector CT angiography meta-analysis. *Radiology* 245:433–439. <https://doi.org/10.1148/RADIOL.2451061280>
- Meyer BC, Werncke T, Foert E et al (2010) Do the cardiovascular risk profile and the degree of arterial wall calcification influence the performance of MDCT angiography of lower extremity arteries? *Eur Radiol* 20:497–505. <https://doi.org/10.1007/S00330-009-1555-7>
- Salimova N, Hinrichs JB, Gutberlet M et al (2022) The impact of the field of view (FOV) on image quality in MDCT angiography of the lower extremities. *Eur Radiol* 32:2875–2882. <https://doi.org/10.1007/s00330-021-08391-x>
- Brockmann C, Jochum S, Sadick M et al (2009) Dual-energy CT angiography in peripheral arterial occlusive disease. *Cardiovasc Intervent Radiol* 32:630–637. <https://doi.org/10.1007/S00270-008-9491-5>
- Gruschwitz P, Petritsch B, Schmid A et al (2023) Noise-optimized virtual monoenergetic reconstructions of dual-energy CT angiographies improve assessability of the lower leg arterial segments in peripheral arterial occlusive disease. *Radiography (Lond)* 29:19–27. <https://doi.org/10.1016/J.RADI.2022.09.002>
- Kosmala A, Weng AM, Schmid A et al (2022) Dual-energy CT angiography in peripheral arterial occlusive disease: diagnostic accuracy of different image reconstruction approaches. *Acad Radiol* 29:S59–S68. <https://doi.org/10.1016/J.ACRA.2020.10.028>
- Willeminck MJ, Persson M, Pourmorteza A et al (2018) Photon-counting CT: technical principles and clinical prospects. *Radiology* 289:293–312
- Flohr T, Petersilka M, Henning A et al (2020) Photon-counting CT review. *Phys Med* 79:126–136. <https://doi.org/10.1016/j.jejmp.2020.10.030>
- Leng S, Bruesewitz M, Tao S et al (2019) Photon-counting detector CT: system design and clinical applications of an emerging technology. *Radiographics* 39:729–743. <https://doi.org/10.1148/rg.2019180115>
- Gutjahr R, Halawish AF, Yu Z et al (2016) Human imaging with photon counting-based computed tomography at clinical dose levels: contrast-to-noise ratio and cadaver studies. *Invest Radiol* 51:421–429. <https://doi.org/10.1097/RLI.0000000000000251>
- Rajagopal JR, Farhadi F, Solomon J et al (2021) Comparison of low dose performance of photon-counting and energy integrating CT. *Acad Radiol* 28:1754–1760. <https://doi.org/10.1016/J.ACRA.2020.07.033>
- Yu Z, Leng S, Kappler S et al (2016) Noise performance of low-dose CT: comparison between an energy integrating detector and a photon counting detector using a whole-body research photon counting CT scanner. *J Med Imaging* 3:043503. <https://doi.org/10.1117/1.JMI.3.4.043503>
- Symons R, Reich DS, Bagheri M et al (2018) Photon-counting CT for vascular imaging of the head and neck: first *in vivo* human results. *Invest Radiol* 53:135. <https://doi.org/10.1097/RLI.0000000000000418>
- Sartoretti T, Wildberger JE, Flohr T, Alkadhi H (2023) Photon-counting detector CT: early clinical experience review. *Br J Radiol*. <https://doi.org/10.1259/BJR.20220544>
- Graafen D, Müller L, Halfmann M et al (2022) Photon-counting detector CT improves quality of arterial phase abdominal scans: a head-to-head comparison with energy-integrating CT. *Eur J Radiol* 156. <https://doi.org/10.1016/J.EJRAD.2022.110514>
- Graafen D, Emrich T, Halfmann MC et al (2022) Dose reduction and image quality in photon-counting detector high-resolution computed tomography of the chest: routine clinical data. *J Thorac Imaging* 37:315–322. <https://doi.org/10.1097/RTI.0000000000000661>
- Sartoretti T, McDermott M, Mergen V et al (2023) Photon-counting detector coronary CT angiography: impact of virtual monoenergetic imaging and iterative reconstruction on image quality. *Br J Radiol* 96. <https://doi.org/10.1259/BJR.20220466>

22. Mergen V, Sartoretto T, Baer-Beck M et al (2022) Ultra-high-resolution coronary CT angiography with photon-counting detector CT: feasibility and image characterization. *Invest Radiol* 57:780–788. <https://doi.org/10.1097/RLI.0000000000000897>
23. Soschynski M, Hagen F, Baumann S et al (2022) High temporal resolution dual-source photon-counting CT for coronary artery disease: initial multicenter clinical experience. *J Clin Med* 11. <https://doi.org/10.3390/JCM11206003>
24. Si-Mohamed SA, Boccalini S, Lacombe H et al (2022) Coronary CT angiography with photon-counting CT: first-in-human results. *Radiology* 303:303–313. <https://doi.org/10.1148/RADIOL.211780>
25. Decker JA, O'Doherty J, Schoepf UJ et al (2023) Stent imaging on a clinical dual-source photon-counting detector CT system—impact of luminal attenuation and sharp kernels on lumen visibility. *Eur Radiol* 33. <https://doi.org/10.1007/S00330-022-09283-4>
26. Rippel K, Decker JA, Wudy R et al (2023) Evaluation of run-off computed tomography angiography on a first-generation photon-counting detector CT scanner— comparison with low-kVp energy-integrating CT. *Eur J Radiol* 158. <https://doi.org/10.1016/J.EJRAD.2022.110645>
27. Gruschwitz P, Hartung V, Kleefeldt F et al (2023) Photon-counting versus energy-integrating detector ct angiography of the lower extremity in a human cadaveric model with continuous extracorporeal perfusion. *Invest Radiol*. <https://doi.org/10.1097/RLI.0000000000000982>
28. Yang Y, Fink N, Emrich T et al (2023) Optimization of kernel type and sharpness level improves objective and subjective image quality for high-pitch photon counting coronary CT angiography. *Diagnostics* 13:1937. <https://doi.org/10.3390/diagnostics13111937>
29. Albrecht T, Meyer BC (2007) MDCT angiography of peripheral arteries: technical considerations and impact on patient management. *Eur Radiol* 17:5–15. <https://doi.org/10.1007/S10406-007-0223-8/METRICS>
30. Fleischmann D, Lammer J (2006) Peripheral CT angiography for interventional treatment planning. *Eur Radiol* 16:M58–M64. <https://doi.org/10.1007/S10406-006-0197-Y/METRICS>
31. Itoga NK, Kim T, Sailer AM et al (2017) Lower extremity computed tomography angiography can help predict technical success of endovascular revascularization in the superficial femoral and popliteal artery. *J Vasc Surg* 66:835–843.e1. <https://doi.org/10.1016/j.jvs.2017.02.031>
32. Al-rudaini HEA, Han P, Liang H (2018) Comparison between computed tomography angiography and digital subtraction angiography in critical lower limb ischemia. *Curr Med Imaging Rev* 15:496–503. <https://doi.org/10.2174/1573405614666181026112532>
33. Mergen V, Eberhard M, Manka R et al (2022) First in-human quantitative plaque characterization with ultra-high resolution coronary photon-counting CT angiography. *Front Cardiovasc Med* 9. <https://doi.org/10.3389/FCVM.2022.981012>
34. McDermott MM, Kramer CM, Tian L et al (2017) Plaque composition in the proximal superficial femoral artery and peripheral artery disease events. *JACC Cardiovasc Imaging* 10:1003–1012. <https://doi.org/10.1016/J.JCMG.2016.08.012>
35. Hartwig JW, Braet DJ, Smith JB et al (2021) Optical coherence tomography and plaque morphology for revascularization of the superficial femoral artery. *Quant Imaging Med Surg* 11:290–299. <https://doi.org/10.21037/QJMS-20-707>
36. Rajendran K, Petersilka M, Henning A et al (2022) First clinical photon-counting detector CT system: technical evaluation. *Radiology* 303:130. <https://doi.org/10.1148/RADIOL.212579>
37. Allmendinger T, Nowak T, Flohr T et al (2022) Photon-counting detector CT-based vascular calcium removal algorithm. *Invest Radiol* 57:399–405. <https://doi.org/10.1097/RLI.0000000000000853>
38. Primrose CW, Hecht EM, Roditi G et al (2021) MR angiography series: fundamentals of contrast-enhanced MR angiography 41:E138–E139. <https://doi.org/10.1148/RG.2021200215>
39. Sharafuddin MJ, Stolpen AH, Sun S et al (2002) High-resolution multi-phase contrast-enhanced three-dimensional MR angiography compared with two-dimensional time-of-flight MR angiography for the identification of pedal vessels. *J Vasc Interv Radiol* 13:695–702. [https://doi.org/10.1016/S1051-0443\(07\)61846-6](https://doi.org/10.1016/S1051-0443(07)61846-6)
40. Mohrs OK, Petersen SE, Heidt MC et al (2011) High-resolution 3D non-contrast-enhanced, ECG-gated, multi-step MR angiography of the lower extremities: comparison with contrast-enhanced MR angiography. *Eur Radiol* 21:434–442. <https://doi.org/10.1007/S00330-010-1932-2/FIGURES/4>
41. Nael K, Krishnam M, Nael A et al (2008) Peripheral contrast-enhanced MR angiography at 3.0T, improved spatial resolution and low dose contrast: initial clinical experience. *Eur Radiol* 18:2893–2900. <https://doi.org/10.1007/S00330-008-1074-Y/TABLES/4>

## Publisher's Note

Springer Nature remains neutral with regard to jurisdictional claims in published maps and institutional affiliations.